RSC Advances

PAPER

View Article Online
View Journal | View Issue

Cite this: *RSC Adv.*, 2026, **16**, 27531

Enhanced heavy metal removal from produced water using metal-incorporated iron oxyhydroxide (FeO(OH)) nanomaterials: adsorption kinetics and isotherm studies

S. Said, * H. H. El-Maghrabi, M. Riad and S. Mikhail

Environmental contamination with heavy metal ions poses a major public health challenge, particularly groundwater contamination affecting drinking, agricultural, and industrial water supplies. Goethite (FeO(OH)) and metal-incorporated goethite (Ca, Co, Mn, Al) nanomaterials were synthesized *via* simple precipitation (pH = 12, aging time 7 days) for adsorptive removal of cadmium and chromium ions. Samples were characterized by XRD, FTIR, HR-TEM, N_2 adsorption–desorption isotherms, and thermal analyses. Results showed that metal incorporation increased surface hydroxyl group content relative to pure goethite. Al incorporation dispersed the goethite needles, reducing their length and width compared to other metal-incorporated variants. Al-goethite achieved the highest adsorption capacity, improving from 72.9 to 86 mg L^{-1} for Cr and 28 to 38 mg L^{-1} for Cd. Adsorption kinetics followed a pseudo-second-order model, confirming chemisorption. Cd adsorption obeyed the Langmuir isotherm ($R^2 \approx 0.99$), indicating monolayer formation on the predominant goethite faces (001 and 010), while Cr adsorption followed both Langmuir and Freundlich models, suggesting mono- and/or multilayer formation. Goethite nanomaterials demonstrated high remediation efficiency for complete heavy metal removal from produced water samples, confirming their promise as effective adsorbents.

Received 3rd May 2026
Accepted 18th May 2026

DOI: 10.1039/d6ra03786k

rsc.li/rsc-advances

1. Introduction

Groundwater constitutes approximately one-third of the world's accessible freshwater resources and serves as a critical supply for drinking, agricultural, and industrial purposes. However, increasing anthropogenic activities particularly industrial discharge have led to the progressive contamination of groundwater with heavy metal ions, posing significant risks to both ecosystem integrity and human health.[1,2] Heavy metals are broadly defined as metallic elements with densities exceeding 5 g cm^{-3} and atomic weights in the range of 63.5–200.6 g mol^{-1}.[3,4] These metals are non-biodegradable and tend to bioaccumulate in living organisms, causing a range of toxic effects even at trace concentrations. Among the most hazardous heavy metal contaminants, cadmium (Cd^{2+}) and hexavalent chromium (Cr(VI)) have attracted considerable regulatory attention due to their documented carcinogenicity, mutagenicity, and nephrotoxicity. In the Delta State region, the maximum detected concentrations of Pb, Cr, Ni, and Cd were 0.18, 0.16, 0.10, and 0.02 mg L^{-1}, respectively all exceeding the limits recommended by the U.S. Environmental Protection Agency (0.006, 0.05, 0.02, and 0.01 mg L^{-1}).[5] These findings highlight the urgent need for effective and economical water treatment strategies. A range of remediation technologies have been applied to remove heavy metals from contaminated water, including chemical precipitation, ion exchange, membrane filtration, electrocoagulation, and adsorption. Among these, adsorption is widely regarded as the most practical approach due to its operational simplicity, design flexibility, cost-effectiveness, and high removal efficiency. The performance of an adsorption process is largely governed by the physicochemical properties of the adsorbent material.[4] In Egypt, rapidly growing water demand driven by population growth, agricultural expansion, and industrialization has intensified interest in the reuse and treatment of non-conventional water sources. Produced water, co-generated with crude oil and natural gas during production operations, represents a major industrial effluent stream that contains complex mixtures of dissolved and dispersed organic compounds alongside heavy metals such as Cd, Cr, Cu, Pb, Hg, Ni, Ag, and Zn.[6] Effective treatment of produced water is essential for enabling its safe reuse in water flooding, irrigation, and industrial processes.

Goethite (FeO(OH)) is one of the most abundant and environmentally stable iron oxyhydroxide minerals. Its structure consists of an orthorhombic lattice with Fe^{3+} occupying octahedral sites within a hexagonally close-packed array of O^{2-} and OH^- anions, giving rise to a high density of reactive surface

Petroleum Refining Division, Egyptian Petroleum Research Institute, Nasr City, 11727, Cairo, Egypt. E-mail: samarsaid@epri.sci.eg; Tel: +20 22531203

Table 1 Comparison of adsorption capacities of FeO(OH)based adsorbents for heavy metal removal reported in the literature

Adsorbent	Metal ion	q_{max} (mg g^{-1})	pH	Isotherm model	Reference
FeO(OH) (G7)	Cr(VI)	72.9	6.0	Langmuir/Freundlich	**This work**
FeO(OH) (G7)	Cd(II)	28.0	6.0	Langmuir	**This work**
Al-goethite (G-Al)	Cr(VI)	86.0	6.0	Langmuir/Freundlich	**This work**
Al-goethite (G-Al)	Cd(II)	38.0	6.0	Langmuir	**This work**
SDS-modified goethite	Pb(II)/Mn(II)	~45–60	~6–7	Langmuir	8 and 9
Mn-doped goethite	Cr(VI)/Cd(II)	~30–50	~5–7	Langmuir	21
Zr-CuO/α-FeOOH	As(V)	~35–55	~5–7	Langmuir	12
Pure goethite (lit.)	Cr(VI)	20–65	4–7	Langmuir	25
Pure goethite (lit.)	Cd(II)	15–30	5–7	Langmuir	25

hydroxyl groups.[7] Goethite is distinguished by its unique physicochemical properties, including high specific surface area, abundant oxygen vacancies (O_v), and low synthesis cost. It forms naturally through the oxidative weathering of iron-rich minerals such as fayalite (Fe_2SiO_4) and pyrite (FeS_2), yielding non-stoichiometric goethite with structural defects that enhance surface reactivity and adsorption capacity.[8] Metal doping has emerged as a powerful strategy to further enhance the catalytic and adsorptive performance of goethite by modulating its electronic structure, optimizing oxygen vacancy concentrations, and generating additional active surface sites. Mohammed *et al.*[9,10] demonstrated that goethite and SDS-modified goethite nanomaterials prepared by precipitation exhibited high adsorption capacities for Pb and Mn, attributable to increased surface hydroxyl group density. Liu *et al.*[11] reported that Cu doping in FeOOH synergistically enhanced chlorine activation and degradation of organic pollutants. Li and Bi[12] observed that Mn(III) and Zn(II) substitution in goethite promoted electron transfer and increased oxygen vacancies, thereby enhancing tetracycline degradation. Furthermore, Tao *et al.*[13] demonstrated that Zr-CuO/FeO(OH) composites achieved efficient arsenic removal through cooperative oxidation and adsorption pathways.

In Egypt, rapidly growing water demand driven by population growth, agricultural expansion, and industrialization has intensified interest in the reuse and treatment of non-conventional water sources. Produced water, co-generated with crude oil and natural gas during production operations, represents a major industrial effluent stream that contains complex mixtures of dissolved and dispersed organic compounds alongside heavy metals such as Cd, Cr, Cu, Pb, Hg, Ni, Ag, and Zn.[6] Effective treatment of produced water is essential for enabling its safe reuse in water flooding, irrigation, and industrial processes.

The novelty of the present study lies in the synergistic effect of specific metal ions (Al, Ca, Co, Mn) on the goethite lattice to enhance surface functionality. As demonstrated in Table 1, the Al-incorporated FeO(OH) synthesized in this work shows a superior maximum adsorption capacity for Cr(VI) compared to many recently reported iron-based nanomaterials and composites. This improvement is primarily attributed to the increased density of surface hydroxyl groups and the morphological refinement observed during characterization.

The present study aims to investigate the heavy metal remediation efficiency of previously prepared goethite (G7)[9] and a series of newly synthesized metal-doped goethite samples (Ca-, Al-, Co-, and Mn-goethite) as adsorbents for the removal of divalent cadmium (Cd^{2+}) and hexavalent chromium (Cr(VI)) from aqueous solutions. These two metals were selected based on their high toxicity, global prevalence in industrial effluents, and differing speciation behaviors, which allow for a comprehensive assessment of the adsorbents' versatility. The practical applicability of the optimized adsorbent was further evaluated using real produced water samples from the Gulf of Suez oil fields. Produced water (PW) the aqueous phase co-extracted with crude oil and natural gas during hydrocarbon production, representing the largest waste stream generated by the petroleum industry poses significant environmental challenges due to its complex composition, including elevated concentrations of heavy metals, salinity, and naturally occurring radioactive materials.

2. Experimental

2.1. Preparation of adsorbent samples

2.1.1. Preparation of goethite (G7). Goethite (G7) was synthesized by a precipitation method as previously described.[9] Briefly, 0.1 mol of $Fe(NO_3)_3 \cdot 9H_2O$ was dissolved in 40 mL of distilled water under continuous magnetic stirring. A 6.0 mol L^{-1} KOH solution was added dropwise to adjust the pH to 12, and the resulting suspension was aged for 7 days at ambient temperature (~25 °C). The precipitate was collected by centrifugation at 3000 rpm for 5 min, washed repeatedly with distilled water to remove residual ions, and dried overnight at 80 °C.

2.1.2. Preparation of metal-incorporated goethite samples. Metal-doped FeO(OH) samples were prepared by incorporating 5 wt% of Ca, Al, Co, or Mn into the G7 matrix *via* an impregnation–precipitation method. The metal precursors used were $Ca(NO_3)_2 \cdot 4H_2O$, $Al(NO_3)_3 \cdot 9H_2O$, $Co(NO_3)_2 \cdot 6H_2O$, and $Mn(CH_3COO)_2$, respectively. The metal-incorporated samples were prepared by adding the required amount of metal precursors (nitrate salts) to the iron solution prior to precipitation, ensuring that the dopants were integrated into the crystal lattice during the 7 day aging process. For each preparation, 2.5 g of G7 was dispersed in 40 mL of distilled water under stirring, followed by dropwise addition of 6.0 mol L^{-1} KOH to adjust the pH to 12. The suspension was aged for 1 h at room temperature, centrifuged at 3000 rpm for 5 min, washed

thoroughly with distilled water, and dried overnight at 80 °C. The resulting metal-incorporated FeO(OH) samples are designated as G-Ca, G-Al, G-Co, and G-Mn, respectively.

2.2. Characterization of the prepared adsorbents

The structural and physicochemical properties of the prepared samples were evaluated using a suite of analytical techniques. X-ray diffraction (XRD) analysis was performed on a Shimadzu XRD-6000 diffractometer (Japan) equipped with CuKα radiation (λ = 1.5406 Å), scanning over the 2θ range of 4°–80° with an increment of 0.028° min^{-1}. Fourier-transform infrared (FTIR) spectra were recorded on a PerkinElmer Spectrum-1 spectrometer in the range of 400–4000 cm^{-1} at a resolution of 4 cm^{-1}. Morphological characterization was carried out using a JEOL JEM-2100F high-resolution transmission electron microscope (HR-TEM) operating at 200 kV. Textural properties were determined from N_2 adsorption–desorption isotherms measured at −196 °C using a NOVA 3200S automated gas sorption analyzer (Quantachrome Corporation). Specific surface areas were calculated by the Brunauer–Emmett–Teller (BET) method, and pore size distributions were obtained from the Barrett–Joyner–Halenda (BJH) method applied to the desorption branch of the isotherm. Thermal behavior was examined by differential thermal analysis (DTA) and thermogravimetric analysis (TGA). Zeta potential and hydrodynamic particle size were determined by dynamic light scattering.

2.3. Adsorption experiments

Stock solutions of Cd(II) and Cr(VI) were prepared by dissolving the corresponding analytical-grade salts in distilled water to obtain concentrations in the range of 25–200 mg L^{-1}. Batch adsorption experiments were conducted by adding a known mass of adsorbent (0.15–0.6 g L^{-1}) to 25 mL of metal ion solution at the desired pH (3–10) and agitating at 200 rpm for 15–120 min. The initial pH was adjusted using dilute HCl or NaOH solutions. After equilibration, the suspension was centrifuged, and the residual metal concentration in the supernatant was determined by flame atomic absorption spectrophotometry (FAAS, Zenit 700p) according to ASTM D4691. The equilibrium adsorption capacity (q_e, mg g^{-1}) was calculated as follows:

$$q_e\left(\text{mg g}^{-1}\right) = \frac{(C_i - C_e)V}{w} \quad (1)$$

where C_i and C_e (mg L^{-1}) are the initial and equilibrium metal ion concentrations, respectively; V (L) is the volume of the solution; and W (g) is the dry mass of the adsorbent.

Adsorption kinetics were modeled using pseudo-first-order (PFO) and pseudo-second-order (PSO) equations. The PFO rate expression[14] is given by:

$$\frac{dq_t}{dt} = k_1(q_e - q_t) \quad (2)$$

Integrating eqn (2) with boundary conditions $q_t = 0$ at t = 0 yields:

$$\ln(q_e - q_t) = \ln q_e - k_1 t \quad (3)$$

Table 2 Chemical composition of the produced water samples used in this study

Parameter	Produced water 1	Produced water 2
Specific gravity	1.0716	1.000133
Density (g L^{-1})	1.07062	1.00034
pH	7.36	6.75
Chromium (mg L^{-1})	1.8	Nil
Manganese (mg L^{-1})	1.17	0.0062
Cadmium (mg L^{-1})	9.7	0.8634
Lead (mg L^{-1})	19.95	0.7337

where q_t and q_e (mg g^{-1}) are the amounts of metal adsorbed at time t and at equilibrium, respectively, and k_1 (min^{-1}) is the PFO rate constant.

The PSO model is expressed as:

$$\frac{dq_t}{dt} = k_2(q_e - q_t) \quad (4)$$

which, upon integration, gives the linearized form:

$$\frac{t}{q_t} = \frac{1}{k_2 q_e^2} + \frac{t}{q_e} \quad (5)$$

where k_2 (g mg^{-1} min^{-1}) is the PSO rate constant. Model suitability was evaluated by comparing the correlation coefficients (R^2) and by assessing the agreement between calculated ($q_{e,cal}$) and experimental ($q_{e,exp}$) equilibrium capacities.

2.4. Analysis of produced water samples

Two produced water samples co-generated from oil-field operations in the Gulf of Suez were provided for evaluation (Table 2). Prior to analysis, the samples were filtered through ashless filter paper (Whatman No. 42). Anion and cation concentrations were determined by ion chromatography (Dionex ICS-1100, equipped with AS9 and CS12 columns) according to ASTM D-4327 and D-6919, respectively. Heavy metal concentrations were measured by FAAS according to ASTM D4691. It should be noted that the produced water treatment experiments were conducted as single measurements ($n = 1$). The absence of replicate statistical data is acknowledged as a limitation of the present study. Results are therefore reported conservatively as removal to below the FAAS instrument detection limit, rather than as statistically confirmed complete removal. Future work will incorporate triplicate measurements with full statistical reporting to provide rigorous quantitative validation of the removal efficiencies reported herein.

3. Results and discussion

3.1. Structural characterization of metal-incorporated goethite

The previously synthesized goethite sample (G7)[9] was loaded with Ca, Al, Mn, and Co *via* an impregnation method. These metals were deliberately selected as dopants because Al, Mn, and Zn commonly occur as trace impurities in natural goethite formed under varying environmental conditions, and their

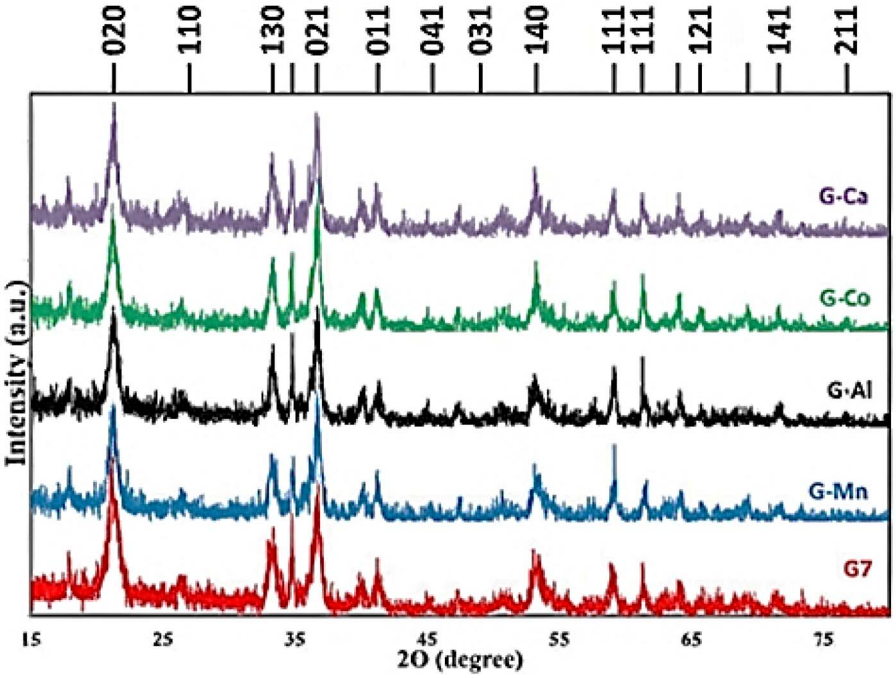

Fig. 1 X-ray diffraction patterns of pristine FeO(OH) (G7) and metal-incorporated goethite samples.

incorporation is known to influence the structural, surface, and adsorption properties of synthetic goethite.

3.1.1. X-ray diffraction analysis. The XRD patterns of pristine goethite (G7) and the metal-incorporated goethite samples are shown in Fig. 1. All diffraction peaks at $2\theta = 21.44°$, 33.20°, 34.96°, 36.91°, 38.5°, 40.17°, 41.29°, 45.29°, 47.49°, 50.85°, 53.36°, 55.60°, 61.40°, and 64.18° were assigned to FeO(OH) (JCPDS 81-0464),[9] confirming that the goethite crystal structure was retained in all doped samples. A notable decrease in peak intensities was observed upon metal incorporation, indicative of reduced crystallinity and increased structural disorder. With the exception of Ca-goethite, no additional diffraction peaks attributable to secondary metal oxide or hydroxide phases were detected, suggesting that the dopant ions were successfully incorporated into the goethite lattice. The systematic decrease in XRD peak intensities upon metal incorporation (Table 3) reflects a progressive reduction in crystallinity and increase in structural disorder, which has direct implications for adsorption performance. Reduced crystallinity in goethite is associated with a higher density of structural defects, edge dislocations, and unsatisfied surface bonds all of which generate additional reactive surface sites for metal ion complexation.[15] This is evidenced by the inverse relationship between crystallinity and adsorption capacity observed across the sample series: G-Ca, which retained the lowest relative peak intensity (69.05%, Table 3), might be expected to show enhanced reactivity; however, its adsorption performance was the lowest among doped samples, confirming that crystallinity alone does not govern adsorption capacity, and that phase purity specifically the formation of $CaCO_3$ secondary phases that block active hydroxyl sites is an equally critical determinant. The peak broadening quantified by FWHM values (Table 3) provides additional mechanistic insight. The progressive increase in FWHM from G7 (0.315°) to G-Ca (0.370°) reflects decreasing coherent scattering domain sizes upon metal incorporation, consistent with the disruption of long-range crystalline order by dopant ions. For G-Al, the FWHM of 0.358° combined with the shift to higher *d*-spacing (4.21 Å *vs.* 4.18 Å for G7) confirms successful lattice incorporation of Al^{3+} at substitutional Fe^{3+} sites, which expands the unit cell and generates additional structural hydroxyl groups accessible for surface complexation. This crystallographic evidence directly supports the superior adsorption capacity of G-Al (q_m = 86 mg L^{-1} for Cr(VI) and 38 mg L^{-1} for Cd(II)), as each substituted Al^{3+} site creates a local charge imbalance and bond distortion that enhances the reactivity of neighboring surface hydroxyl groups toward incoming metal ions. For G-Mn, the negligible change in *d*-spacing (4.19 Å) despite Mn incorporation suggests that Mn substitution at Fe^{3+} sites is limited, with excess Mn likely segregating as amorphous MnO_x surface species, a conclusion supported by the BET data showing the lowest pore volume among all samples ($V_p = 0.1929$ cm^3 g^{-1}, Table 4) due to pore blockage by these surface precipitates. This structural interpretation directly accounts for the intermediate adsorption performance of G-Mn,

Table 3 X-ray diffraction parameters for FeO(OH) (G7) and metal-doped goethite samples

Sample	2θ (°)	*d*-Spacing (Å)	Height	FWHM	Int. (%)
G7	21.24	4.18	64.58	0.315	100.00
G-Mn	21.22	4.19	58.30	0.321	90.25
G-Al	21.19	4.21	52.10	0.358	80.71
G-Co	21.30	4.17	49.80	0.342	77.10
G-Ca	21.38	4.15	44.60	0.370	69.05

Table 4 Textural properties, particle characteristics, and maximum adsorption capacities of G7 and metal-incorporated goethite samples

Sample	S_{BET} ($m^2\ g^{-1}$)	r_H (nm)	V_p ($cm^3\ g^{-1}$)	Particle size (nm)	Zeta potential (mV)	q_m Cr(VI) (mg g^{-1})	q_m Cd(II) (mg g^{-1})
G7	143	0.96	0.2498	2305	5.5	72.9	28.0
G-Ca	122.1	1.0866	0.256	68.06	24.9	71.0	28.0
G-Al	96.82	1.6837	0.232	37.8	40.1	86.0	38.0
G-Co	94.6	1.217	0.237	91.3	20.5	82.0	36.0
G-Mn	85.94	1.2264	0.1929	77.5	22.3	76.0	32.0

which benefits from some additional surface sites generated by lattice disorder but is simultaneously penalized by reduced pore accessibility.

3.1.2. FTIR spectroscopy. The FTIR spectra provide critical quantitative insight into the surface chemistry of the prepared adsorbents that directly explains the observed adsorption performance hierarchy. The FTIR spectra of G7 and the metal-incorporated goethite samples are presented in Fig. 2. The characteristic absorption bands of FeO(OH) were observed at approximately 890 and 795 cm^{-1}, corresponding to the in-plane and out-of-plane bending vibrations of O–H groups coordinated to Fe^{3+}, and at ~630 cm^{-1} attributed to Fe–O–H deformation modes. The bands at ~3120 and ~3400 cm^{-1} correspond to O–H stretching vibrations of surface and structural hydroxyl groups, respectively.[16] The intensity of the O–H stretching bands at ~3120 and ~3400 cm^{-1} serves as a proxy for the relative density of structural and surface hydroxyl groups the primary active sites for heavy metal uptake *via* inner-sphere complexation and ligand exchange. The systematic enhancement of these bands upon metal incorporation, most pronounced for G-Al, directly correlates with the adsorption capacity order: G-Al > G-Co > G-Mn > G-Ca > G7 (ref. 17) (Section 3.2.6). For G-Al specifically, the marked increase in O–H band intensity relative to G7 is attributed to two synergistic effects of Al^{3+} incorporation; the smaller ionic radius of Al^{3+} (0.53 Å *vs.* Fe^{3+} at 0.65 Å) creates local lattice distortions that expose a greater number of edge and corner hydroxyl groups on the goethite surface; and the higher charge density of Al^{3+} relative to Fe^{3+} polarizes the coordinated hydroxyl groups more strongly, increasing their reactivity toward electrophilic metal ions such as Cd^{2+} and toward anion exchange with chromate (CrO_4^{2-}). This dual effect of Al^{3+} on hydroxyl group density and reactivity provides a direct mechanistic explanation for the 18% improvement in Cr(VI) capacity (72.9 → 86 mg L^{-1}) and the 36% improvement in Cd(II) capacity (28 → 38 mg L^{-1}) relative to pristine G7. The Fe–O–H deformation bands at ~890 and ~795 cm^{-1}, corresponding to in-plane and out-of-plane bending of surface hydroxyl groups coordinated to Fe^{3+}, showed a systematic shift and broadening upon metal incorporation. For G-Al, the broadening of these bands is consistent with the heterogeneous local coordination environment created by Al^{3+} substitution, where surface hydroxyl groups are coordinated to both Fe^{3+} and Al^{3+} centers with different Lewis acid strengths generating a distribution of binding site energies that collectively enhance the adsorption affinity for both Cd^{2+} and CrO_4^{2-}. This interpretation is consistent with the Freundlich isotherm applicability for Cr(VI) (R^2 = 0.97–0.99, Table 7), which describes adsorption on energetically heterogeneous surfaces.

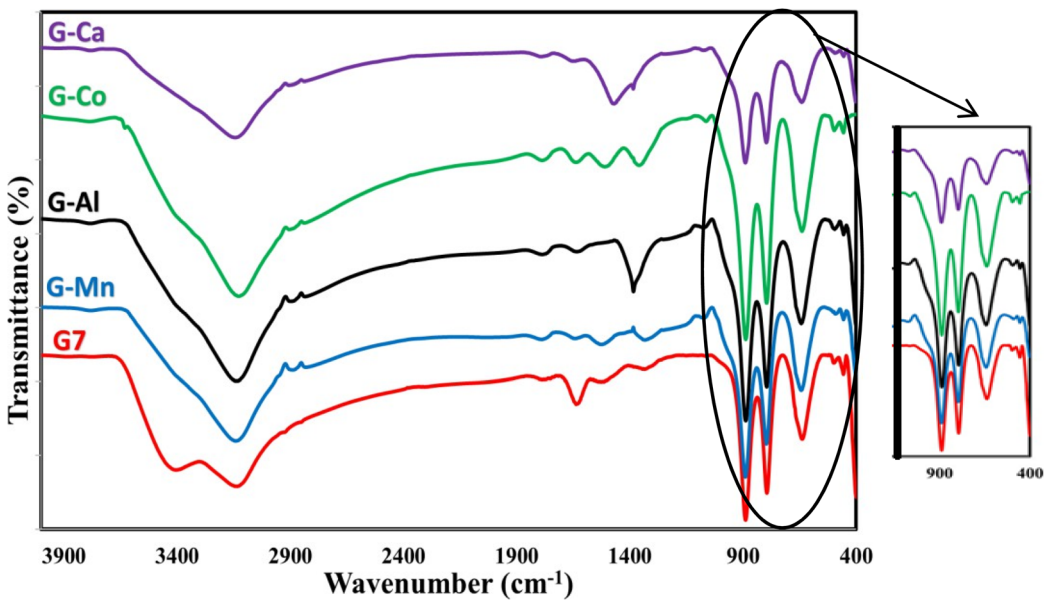

Fig. 2 FTIR spectra of G7 and metal-incorporated G7 samples.

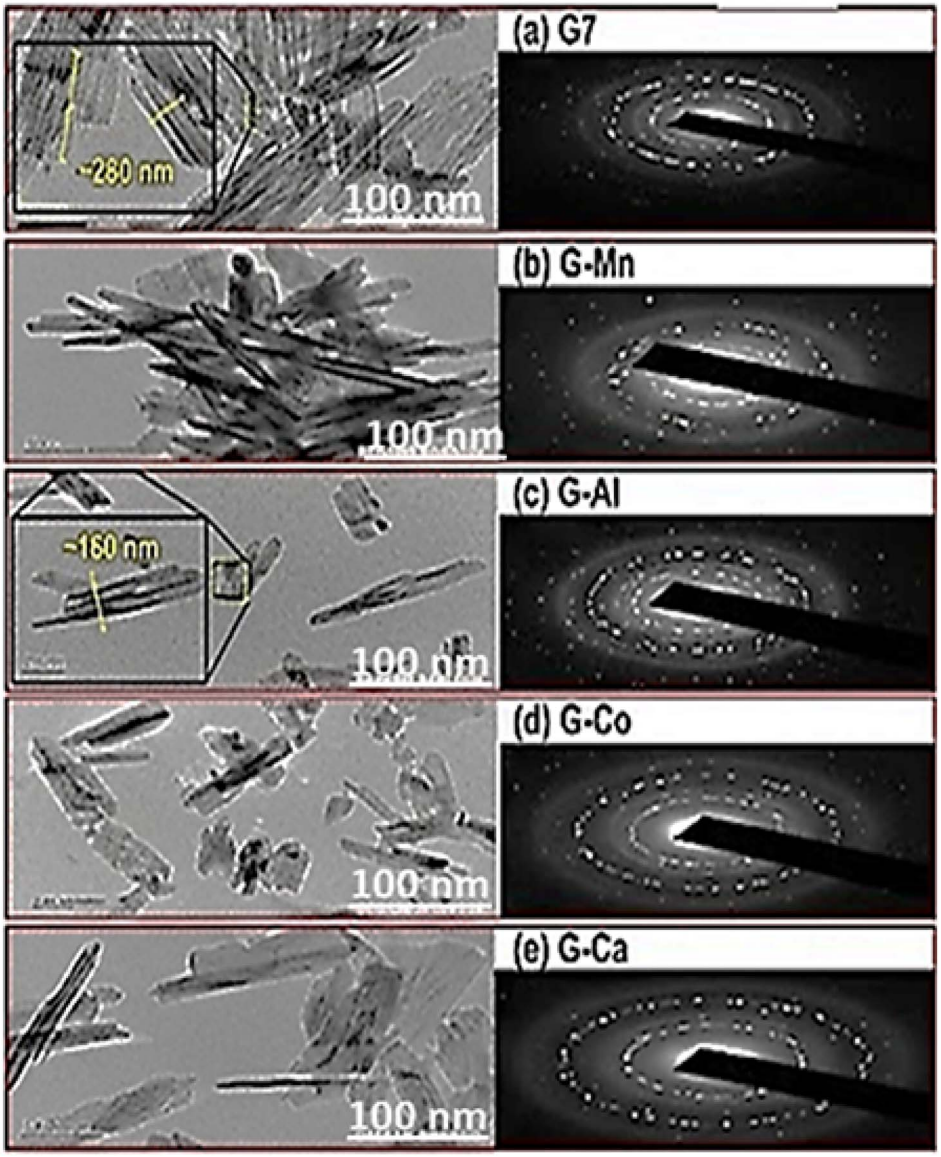

Fig. 3 HR-TEM images of (a) G7, (b) G-Al, (c) G-Co, (d) G-Mn, and (e) G-Ca.

For G-Ca, the emergence of the C–O stretching band at ~870 cm^{-1} attributable to $CaCO_3$ (ref. 18) is particularly significant from an adsorption performance perspective. The formation of this secondary carbonate phase effectively consumes surface Ca^{2+} species that would otherwise contribute positively charged sites for anionic Cr(VI) adsorption, and simultaneously blocks a fraction of the goethite hydroxyl groups from participating in surface complexation. The FTIR evidence for $CaCO_3$ formation thus provides a direct spectroscopic explanation for the lowest adsorption capacity among the doped samples observed for G-Ca, complementing the XRD and BET data. For G-Mn, the moderate enhancement of O–H bands relative to G7 lower than that observed for G-Al and G-Co is consistent with the partial segregation of Mn as MnO_x[19] surface species rather than full lattice incorporation. MnO_x species, while introducing additional surface oxygen functionality, carry a strong polarizing effect that generates net negative surface charge under the adsorption conditions (pH 6.0), suppressing the electrostatic attraction of anionic Cr(VI) species and reducing overall adsorption capacity relative to G-Al and G-Co.

3.1.3. HR-TEM analysis. The morphology of the prepared samples was examined by HR-TEM (Fig. 3). Pristine FeO(OH) (G7) exhibited the characteristic needle-like (acicular) crystal morphology with average lengths of ~200–300 nm and widths of ~20–40 nm. Upon metal incorporation, notable morphological changes were observed: Al-FeO(OH)(G-Al) showed the most significant morphological transformation, with a marked reduction in needle length and width and more uniform particle dispersion. This is attributed to the incorporation of small Al^{3+} ions (ionic radius = 0.53 Å) into and between the FeO(OH)octahedral layers, disrupting crystal growth along the principal axis and promoting lateral dispersion of the needle-

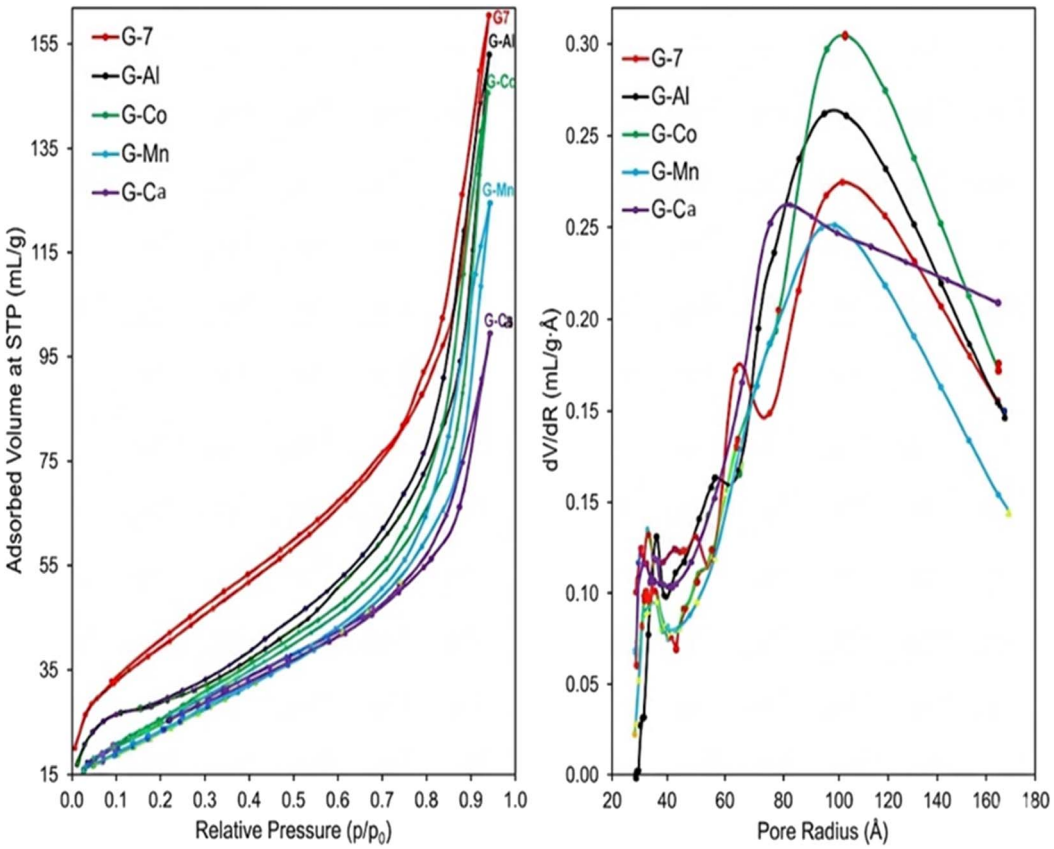

Fig. 4 N_2 adsorption–desorption isotherms of G7 and metal-incorporated goethite samples. Inset: BJH pore size distribution curves.

like crystals. This dispersion resulted in a substantially higher specific surface area for G-Al, as confirmed by BET analysis (Section 3.1.4). Co- and Mn-doped samples also exhibited shorter needles compared to G7, while Ca-doped FeO(OH) showed partial aggregation of needle clusters, consistent with the lower zeta potential values recorded for this sample.

3.1.4. N_2 Adsorption–desorption and BET analysis. The N_2 adsorption–desorption isotherms and BJH pore size distributions of the prepared samples are shown in Fig. 4. All samples exhibited Type IV isotherms with H3-type hysteresis loops (IUPAC classification), characteristic of mesoporous materials with slit-shaped pores formed by aggregates of plate-like particles consistent with the acicular goethite morphology observed by HR-TEM (Section 3.1.3). The BET surface area (S_{BET}), mean hydraulic pore radius (r_H), total pore volume (V_p), hydrodynamic particle size, and zeta potential for all samples are summarised in Table 4, alongside the corresponding maximum adsorption capacities for Cr(VI) and Cd(II). Pristine G7 exhibited the highest surface area (143 $m^2\ g^{-1}$) and pore volume (0.2498 $cm^3\ g^{-1}$) among all samples. Upon metal incorporation, a systematic decrease in S_{BET} was observed, following the order: G7 (143 $m^2\ g^{-1}$) > G-Ca (122.1 $m^2\ g^{-1}$) > G-Al (96.82 $m^2\ g^{-1}$) > G-Co (94.6 $m^2\ g^{-1}$) > G-Mn (85.94 $m^2\ g^{-1}$). This trend reflects the partial occupation of goethite surface and pore channels by the incorporated metal species, which reduces the net accessible surface area relative to the unmodified material. Notably, despite possessing a lower absolute surface area than G7, G-Al achieved the highest adsorption capacities for both Cr(VI) (q_m = 86 mg L^{-1}) and Cd(II) (q_m = 38 mg L^{-1}). This apparent decoupling of surface area and adsorption capacity is explained by two complementary factors, the largest mean pore radius among all doped samples (r_H = 1.6837 nm for G-Al), which facilitates intraparticle diffusion of metal ions to interior binding sites; and the markedly enhanced surface hydroxyl group density generated by Al^{3+} incorporation (confirmed by FTIR, Section 3.1.2) and the higher ionic potential of Al^{3+} relative to Fe^{3+}, which strengthens surface complexation of both Cd^{2+} and CrO_4^{2-}. These results demonstrate that surface chemistry and pore accessibility rather than raw surface area alone are the primary determinants of adsorption performance in this material system. G-Mn exhibited the lowest surface area (85.94 $m^2\ g^{-1}$) and pore volume (0.1929 $cm^3\ g^{-1}$) among all samples, attributable to partial blockage of mesopore channels by MnO_x surface species, which restrict intraparticle diffusion pathways and reduce the density of accessible active sites consistent with its comparatively lower adsorption performance. G-Ca showed an intermediate surface area (122.1 $m^2\ g^{-1}$) but the lowest adsorption capacity among the doped samples, due to the formation of $CaCO_3$ secondary phases (confirmed by XRD and FTIR) that partially occlude active surface hydroxyl groups. The zeta potential data further corroborate these trends, G-Al exhibited the highest zeta

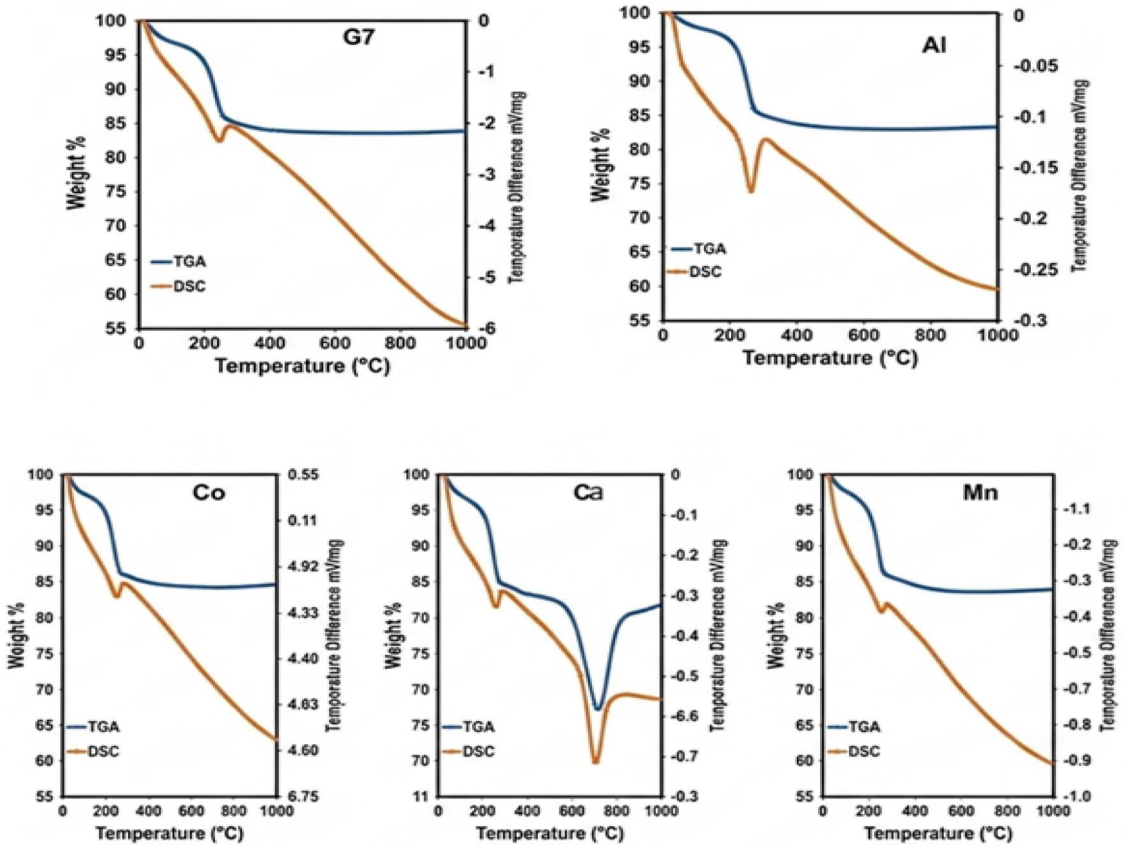

Fig. 5 DTA and TGA profiles of G7 and metal-incorporated goethite samples.

potential (+40.1 mV) and the smallest particle size (37.8 nm), reflecting superior colloidal stability and dispersion arising from the uniform distribution of Al^{3+} across the goethite surface, which amplifies electrostatic repulsion between particles and suppresses agglomeration.

3.1.5. Thermal analysis (DTA/TGA). Thermal decomposition profiles of the goethite samples are presented in Fig. 5, with corresponding weight loss data summarized in Table 5. All samples displayed three main weight loss events. Weight loss of 2.7–3.5% attributed to the desorption of physisorbed and weakly bound surface water at 30–125 °C. The most significant weight loss (10.85–11.96%), corresponding to the structural dehydroxylation of goethite ($FeO(OH) \rightarrow \alpha\text{-}Fe_2O_3$) and the loss of hydroxyl groups associated with the incorporated metal species (125–280 °C). A minor weight loss (1.5–2.2%) at temperature range 280–1000 °C due to the decomposition of residual structural hydroxyl groups from Mn, Co, or Al hydroxide phases. For G-Ca, an additional weight loss at 280–580 °C was attributed to the thermal decomposition of $CaCO_3$ to $CaO + CO_2$.[20] G-Al showed the highest total weight loss (16.84%), consistent with a greater abundance of structural hydroxyl groups compared to the other samples, supporting the FTIR findings and further confirming the enhanced surface reactivity of this material.

3.1.6. Zeta potential and particle size analysis. Zeta potential and hydrodynamic particle size data for the metal-incorporated FeO(OH)samples are presented in Table 4. Metal incorporation systematically increased the zeta potential relative to pristine G7 ($\zeta = +5$ mV), indicating enhanced surface charge stability. The most dramatic improvement was observed for G-Al, which exhibited a zeta potential of +40.1 mV and a markedly reduced particle size of 37.8 nm, compared to 2350 nm for G7. The high zeta potential of G-Al is attributed to the uniform distribution of Al^{3+} ions across the FeO(OH) surface

Table 5 Thermogravimetric weight loss data for G7 and metal-incorporated goethite samples

Sample	Temperature range (°C)	Weight loss (%)	Total loss (%)
G7	30–125/125–265/265–1000	3.50/10.85/1.90	16.25
G-Mn	30–125/125–280/300–1000	2.72/11.33/1.96	16.13
G-Al	30–140/140–280/280–1000	2.69/11.96/2.18	16.84
G-Co	30–140/140–280/280–1000	3.05/10.94/1.54	15.50
G-Ca	25–125/125–280/280–580/580–1000	3.33/11.68/2.84/0.73	18.59

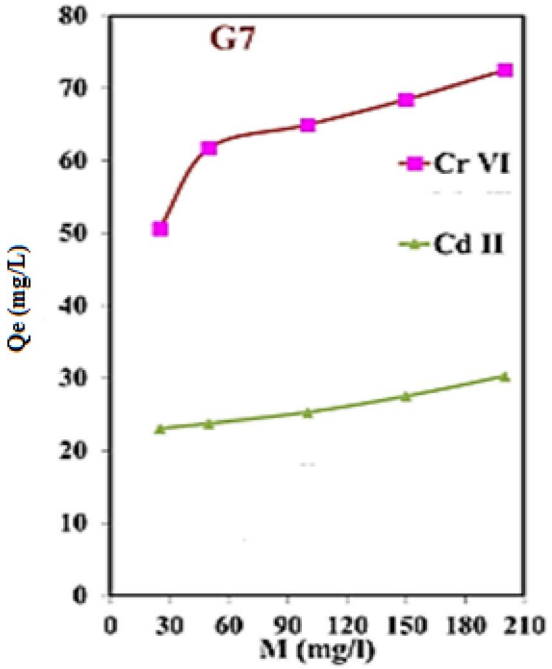

Fig. 6 Effect of contact time on the adsorption capacity of G7 for Cd(II) and Cr(VI) (conditions: $C_0 = 50$ mg L^{-1}, pH 6.0, adsorbent dose = 10 mg).

and within the interstitial spaces of the octahedral layers, generating additional positively charged sites and suppressing particle agglomeration through electrostatic repulsion. In contrast, G-Co exhibited a lower zeta potential (+24.9 mV) and a larger particle size (91.3 nm), consistent with the formation of bidentate binuclear surface complexes by Co species, which reduce surface charge density and promote particle aggregation. G-Mn ($\zeta = +22$ mV, $d = 77$ nm) and G-Ca ($\zeta = +20.5$ mV, $d =$ 68 nm) showed intermediate values, reflecting partial incorporation of these metals into the FeO(OH) structure and concomitant redistribution of surface charge.

3.2. Adsorption performance

The surface chemistry of FeO(OH)adsorption sites is governed by the coordination environment of surface Fe–OH, Fe–O^-, and $FeOH_2^+$ groups, which serve as the primary active sites for toxic metal uptake through electrostatic interactions, ligand exchange, and surface complexation. The adsorption capacities of the prepared FeO(OH)samples for Cd(II) and Cr(VI) were systematically evaluated as a function of contact time, solution pH, adsorbate concentration, temperature, and adsorbent dose. The results are presented in Fig. 6–11.

3.2.1. Effect of contact time. The influence of contact time on the adsorption capacity of G7 for Cd(II) and Cr(VI) is shown in Fig. 6. Experiments were conducted using 10 mg of adsorbent, 25 mL of 50 mg L^{-1} metal solution at pH 6.0 and ambient temperature, with contact times of 15, 30, 45, and 60 min. Adsorption capacity increased continuously with time for both metals, reaching equilibrium within 60 min, after which no significant further uptake was observed. The adsorption capacity at equilibrium was 24 mg L^{-1} for Cd(II) and 62 mg L^{-1} for Cr(VI). The higher adsorption capacity for Cr(VI) under identical conditions reflects the greater affinity of the positively charged goethite surface for anionic chromate species ($HCrO_4^-$, CrO_4^{2-}) at pH 6.0.

3.2.2. Effect of solution pH. The solution pH exerts a profound influence on metal ion speciation and surface charge, and consequently on adsorption capacity. The effect of pH (range: 3–9) on Cd(II) and Cr(VI) adsorption onto G7 was investigated using 10 mg adsorbent in 25 mL of 50 mg L^{-1} metal solution at ambient temperature and 60 min contact time (Fig. 7). For Cd(II), adsorption capacity increased sharply with increasing pH from 3 to 5, and plateaued at ~40 mg L^{-1} in the basic range (pH ≥ 9). At low pH, the FeO(OH)surface is protonated ($FeOH + H^+ \rightarrow FeOH_2^+$), generating a positive surface charge that repels cationic Cd^{2+} species and promotes the formation of weaker outer-sphere complexes. As pH increases, surface deprotonation enhances negative surface charge density, facilitating the formation of stronger inner-sphere monodentate and bidentate complexes with Cd^{2+}. At high pH (≥9), cadmium tends to form tridentate edge-sharing complexes anchored to triply coordinated oxygen sites (Fe_3–O) on the FeO(OH)surface, reaching maximum uptake capacity of ~82 mg L^{-1}. For Cr(VI), a notably different pH-dependence was observed. Adsorption capacity was highest at low pH (~126 mg L^{-1} at pH 3), consistent with the strong electrostatic attraction between anionic chromate species ($HCrO_4^-$, CrO_4^{2-}) and the highly positive FeO(OH) surface charge at acidic pH, and gradually decreased to ~99 mg L^{-1} at pH 9 as the surface charge became less positive and approached the p_{HPZC} of

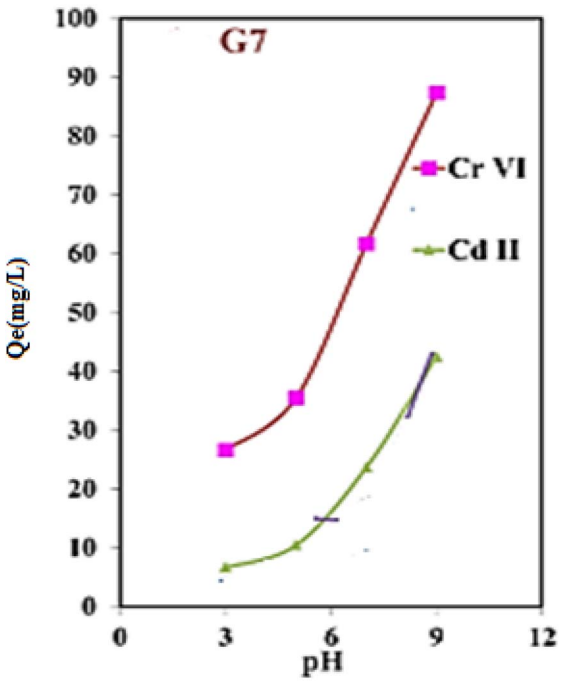

Fig. 7 Effect of solution pH on the adsorption capacity of G7 for Cd(II) and Cr(VI) (conditions: C_0 = 50 mg L^{-1}, adsorbent dose = 10 mg, contact time = 60 min).

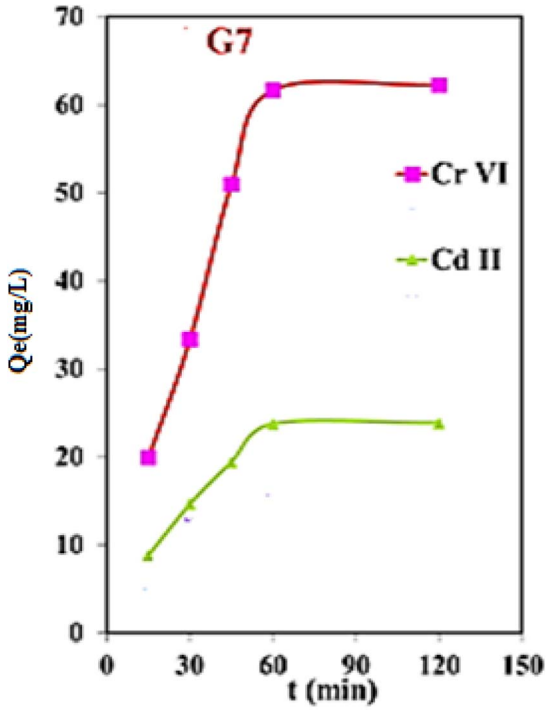

Fig. 8 Effect of initial adsorbate concentration on adsorption capacity of G7 for Cd(II) and Cr(VI) (conditions: pH 6.0, adsorbent dose = 10 mg, contact time = 60 min).

FeO(OH). This inverse pH dependence is fully consistent with the well-established surface complexation mechanism of Cr(VI) on iron oxyhydroxide surfaces.[21] It should be noted that pH-dependent zeta potential measurements were not performed in the present study. However, the surface charge behaviour assumed in the mechanistic discussion is consistent with the well-established pH_{PZC} of FeO(OH)reported in the literature (pH 7.5–9.4;[15,22,23] and is further supported by the static zeta potential data reported in Table 4, which confirm net positive surface charge for all samples at neutral pH. Al substitution has been reported to increase the pH_{PZC} of goethite, consistent with the enhanced positive charge density and superior Cr(VI) adsorption performance observed for G-Al across the full pH range studied. Future work will include systematic pH-dependent zeta potential measurements to provide direct experimental validation of the proposed surface complexation mechanisms.

The pH-dependent adsorption behavior of Cr(VI) is consistent with its well-established aqueous speciation. At acidic pH (<6), Cr(VI) exists predominantly as the monovalent hydrogen chromate anion ($HCrO_4^-$), which is strongly attracted to the protonated, positively charged FeO(OH) surface (p_{HPZC} = 7.5–9.4) through electrostatic interactions. At near-neutral to alkaline pH, the divalent chromate anion (CrO_4^{2-}) becomes the dominant species; however, the increasingly negative surface charge of FeO(OH) at pH > p_{HPZC} progressively reduces electrostatic attraction, leading to the observed decline in Cr(VI) adsorption capacity with increasing pH. This speciation behavior is well-documented in the literature[24] and is fully consistent with our experimental pH-dependence data (Fig. 7).

3.2.3. Effect of initial adsorbate concentration. The effect of initial metal ion concentration (25–200 mg L^{-1}) on the adsorption capacity of G7 was studied at pH 6.0, ambient temperature, and 60 min contact time (Fig. 8). Adsorption capacity for Cd(II) increased gradually with increasing concentration, reaching an equilibrium value of approximately 16 mg L^{-1} at 200 mg L^{-1}. Cr(VI) displayed a markedly higher affinity, with q_e increasing steeply from ~50 mg L^{-1} at 30 mg L^{-1} initial concentration to 74 mg L^{-1} at 200 mg L^{-1}. The progressive increase in adsorption capacity with concentration is attributed to the increased driving force for mass transfer at higher adsorbate concentrations, which promotes partial dissolution of goethite along the preferential (010) and (001) crystal faces, releasing Fe ions that contribute to surface complex formation and subsequent precipitation of metal hydroxides on the adsorbent surface.

3.2.4. Effect of temperature. The influence of reaction temperature (25–70 °C) on the adsorption of Cd(II) and Cr(VI) onto G7 is shown in Fig. 9. For both metals, adsorption capacity decreased with increasing temperature, with Cr(VI) showing a more pronounced temperature sensitivity: q_m decreased sequentially from 62 mg L^{-1} at 25 °C to 31 mg L^{-1} at 70 °C. This inverse relationship between adsorption capacity and temperature indicates that the adsorption process is exothermic in nature, which is consistent with a chemisorption mechanism involving the formation of strong surface complexes. The decrease in adsorption capacity at elevated temperatures may be attributed to enhanced desorption of surface-bound metal species and weakening of the adsorbent–adsorbate bond energy at higher thermal energies.

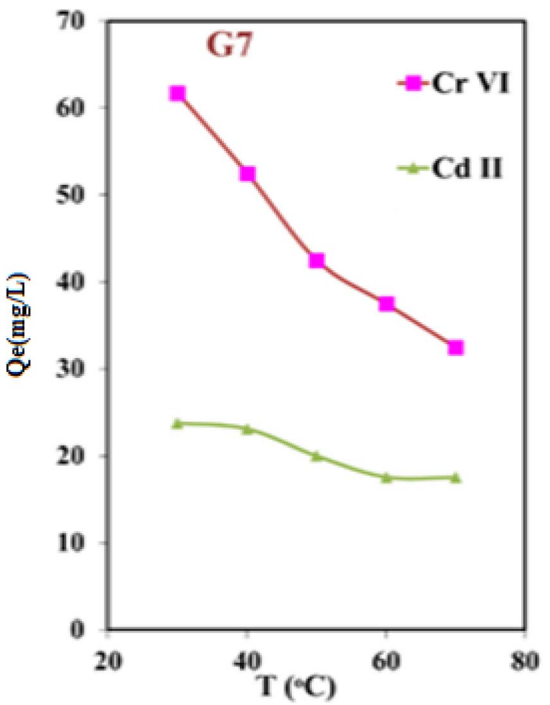

Fig. 9 Effect of reaction temperature on adsorption capacity of G7 for Cd(II) and Cr(VI) (conditions: C_0 = 50 mg L^{-1}, pH 6.0, adsorbent dose = 10 mg, contact time = 60 min).

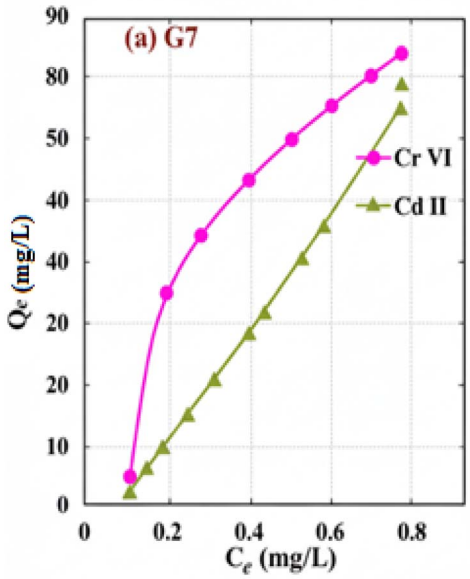

Fig. 10 Effect of adsorbent dose on adsorption capacity of G7 for Cd(II) and Cr(VI) (conditions: $C_0 = 50$ mg L^{-1}, pH 6.0, contact time = 60 min).

3.2.5. Effect of adsorbent dose. The effect of adsorbent dose (0.1–0.6 g L^{-1}) on metal removal efficiency was investigated under standard conditions (C_0 = 50 mg L^{-1}, pH 6.0, 60 min). As shown in Fig. 10, adsorption capacity for both Cd(II) and Cr(VI) increased with increasing adsorbent dose, with Cr(VI) exhibiting a sharper rise: q_m increased from 7 mg L^{-1} at 0.1 g L^{-1} adsorbent dose to 89 mg L^{-1} at 0.6 g L^{-1}. This behavior is consistent with the increased availability of active surface sites for complexation and ligand exchange as more adsorbent is introduced into the system. Beyond a certain dose, however, the marginal increase in adsorption capacity diminishes as interparticle interactions and site saturation become more prevalent.

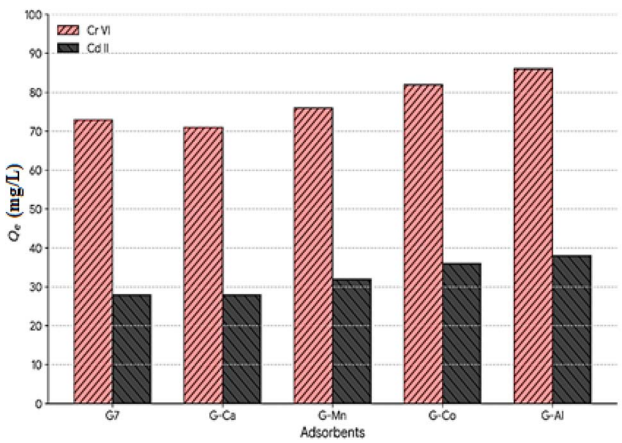

Fig. 11 Comparative histogram of adsorption capacities for Cr(VI) and Cd(II) on G7 and metal-incorporated goethite samples (conditions: C_0 = 50 mg L^{-1}, pH 6.0, adsorbent dose = 10 mg, contact time = 60 min).

3.2.6. Comparative adsorption performance of metal-incorporated goethite samples. The adsorption capacities of G7, G-Ca, G-Co, G-Al, and G-Mn for Cr(VI) and Cd(II) removal under standardized conditions (C_0 = 50 mg L^{-1}, pH 6.0, adsorbent dose = 10 mg, 25 mL solution, ambient temperature, 60 min) are compared histographically in Fig. 11. All metal-incorporated samples outperformed pristine G7, with the adsorption capacity following the order: G-Al > G-Co > G-Mn > G-Ca > G7. G-Al exhibited the highest adsorption capacities (q_m = 86 mg L^{-1} for Cr(VI) and 38 mg L^{-1} for Cd^{2+}), attributable to its higher surface hydroxyl group density (confirmed by FTIR and TGA) and larger mean pore radius (r_H = 1.6837 nm) rather than raw surface area. This distinction surface chemistry over surface area is now presented as a key scientific finding of the study; and also to the higher ionic potential of Al^{3+} relative to Fe^{3+}, which enhances the binding force toward OH^- and metal ions, resulting in more efficient surface complexation. G-Mn showed somewhat lower performance compared to G-Co, likely because MnO_x species on the FeO(OH)surface exert a strong polarizing effect that reduces the affinity of surface oxygen atoms for protons, generating net negative surface charge that suppresses the adsorption of anionic Cr(VI) species. Furthermore, MnO_x may partially obstruct the mesopores of α-FeOOH, limiting intraparticle diffusion and reducing accessible surface area. G-Ca exhibited the lowest capacity among the doped samples, which is attributed to the formation of $CaCO_3$ phases that reduce effective surface charge and block active sites.

3.3. Adsorption kinetics

The kinetics of Cd(II) and Cr(VI) adsorption onto G7 were analyzed using the pseudo-first-order (PFO) and pseudo-second-order (PSO) models to elucidate the rate-limiting step and adsorption mechanism. Model parameters were determined from linearized plots and are summarized in Table 6.

3.3.1. Pseudo-first-order model. The PFO model assumes that the rate of adsorption is proportional to the number of unoccupied surface sites. The linear plot of $\ln(q_e - q_t)$ *versus* t (Fig. S1a & S2a) yielded R^2 values below 0.92 for Cd(II) and Cr(VI) adsorption on G7. Moreover, the calculated equilibrium capacities ($q_{e,cal}$ = 140 mg L^{-1} for Cr(VI) and 28 mg L^{-1} for Cd(II)) diverged significantly from the corresponding experimental values ($q_{e,exp}$ = 61.8 and 24 mg L^{-1}, respectively). This poor agreement indicates that the PFO model is inadequate for describing the adsorption kinetics under the studied conditions, and that the process is not governed by a simple diffusion-controlled mechanism. The divergence (PFO predicts $q_{e,cal}$ = 140–170 mg L^{-1} *vs.* $q_{e,exp}$ = 61–88 mg L^{-1}) is in fact a direct indication that the PFO model is inappropriate for this system and is used as confirmatory evidence that adsorption is not controlled by a simple diffusion-limited (physisorption) mechanism. This overestimation, arising because the PFO model cannot properly describe chemisorption systems with nonlinear approach to equilibrium, is now cited to support the selection of the PSO model as the appropriate kinetic description.

Table 6 Pseudo-first-order and pseudo-second-order kinetic parameters for Cd(II) and Cr(VI) adsorption

Adsorbent	Metal	q_e,exp (mg L^{-1})	PFO: $q_{e,cal}$	k_1 (min^{-1})	R^2	PSO: $q_{e,cal}$	k_2 (g L^{-1} min^{-1})	R^2
G7	Cr	61.8	140	0.058	0.92	87.7	0.000453	0.92
G7	Cd	24	28	0.055	0.92	31	0.001843	0.96
G-Ca	Cr	71	148	0.062	0.93	74.2	0.004984	0.98
G-Ca	Cd	28	32	0.058	0.91	29.5	0.010546	0.99
G-Mn	Cr	76	155	0.065	0.94	79.1	0.005166	0.99
G-Mn	Cd	32	38	0.061	0.92	33.8	0.008766	0.99
G-Co	Cr	82	162	0.068	0.95	85.3	0.004855	0.99
G-Co	Cd	36	44	0.064	0.93	37.4	0.011459	0.99
G-Al	Cr	88	170	0.072	0.96	87.7	0.003524	0.99
G-Al	Cd	42	50	0.069	0.94	31	0.004840	1.00

3.3.2. Pseudo-second-order model. The PSO model was found to provide a significantly better description of the experimental data.[25] Linear plots of t/q_t *versus* t (Fig. S1b) yielded R^2 values of approximately 0.99 for both metals, with calculated equilibrium capacities ($q_{e,cal}$ = 87.7 mg L^{-1} for Cr(VI) and 31 mg L^{-1} for Cd(II)) in close agreement with the experimental data (Table 6). The applicability of the PSO model across all adsorbent samples (G7, G-Ca, G-Mn, G-Co, and G-Al), with $R^2 \geq 0.98$, suggests that the adsorption of Cr(VI) and Cd(II) on FeO(OH)-based adsorbents is a rate-limiting step involving electronic forces or chemical bonding, involving the sharing or exchange of electrons between the metal ions and the reactive surface hydroxyl groups of goethite. The adsorption capacity followed the order G-Al > G-Co > G-Mn > G-Ca > G7, consistent with the comparative performance data in Section 3.2.6.

3.4. Adsorption isotherm analysis

Adsorption equilibrium data were analyzed using the Langmuir and Freundlich isotherm models to elucidate the nature of the adsorption process and the distribution of active sites on the adsorbent surface. Experiments were conducted over an initial concentration range of 25–200 mg L^{-1} at ambient temperature and with 10 mg of adsorbent. The exclusive Langmuir fit for Cd(II) reflects the homogeneous inner-sphere complexation of a single dominant aqueous species (Cd^{2+}) at discrete surface hydroxyl sites of uniform coordination geometry. By contrast, the dual Langmuir–Freundlich applicability for Cr(VI) is attributed to the simultaneous presence of multiple adsorption modes (outer-sphere electrostatic and inner-sphere ligand exchange) and the concentration-dependent speciation of chromate between $HCrO_4^-$ and CrO_4^{2-} both of which introduce energetic heterogeneity at the FeO(OH) surface.[21,26]

3.4.1. Langmuir isotherm. The Langmuir model assumes monolayer adsorption onto a homogeneous surface with a finite number of identical, energetically equivalent binding sites, with no lateral interactions between adsorbed species.[27] The non-linear Langmuir equation is:

$$q_e = \frac{q_m b C_e}{1 + b C_e} \quad (6)$$

which is linearized as:

$$\frac{C_e}{q_e} = \frac{1}{k_L q_m} + \frac{C_e}{q_m} \quad (7)$$

where q_m (mg g^{-1}) is the maximum monolayer adsorption capacity and K_L (L mg^{-1}) is the Langmuir affinity constant. The linearity of C_e/q_e *versus* C_e plots (Fig. S3) and high R^2 values (Table 7) confirm the applicability of the Langmuir model for Cd(II) and Cr(VI) adsorption on all samples. The adsorption of Cd(II) on G7 obeyed the Langmuir isotherm with $R^2 = 0.99$ and q_m = 28 mg g^{-1}, indicating uniform monolayer formation predominantly on the (001) and (010) crystal faces of goethite. The near-perfect fit of the Langmuir model for G-Al ($R^2 = 1.00$, q_m = 38 mg L^{-1} for Cd^{2+}; q_m = 86 mg L^{-1} for Cr(VI)) confirms that Al doping creates a more homogeneous distribution of active adsorption sites on the goethite surface. The maximum monolayer capacities followed the order: G-Al > G-Co > G-Mn > G-Ca > G7.

Table 7 Langmuir and Freundlich isotherm parameters for Cd(II) and Cr(VI) adsorption on G7 and metal-incorporated goethite samples

Adsorbent	Metal	Langmuir q_m (mg L^{-1})	K_L (L mg^{-1})	R^2	Freundlich K_F	n	R^2
G7	Cr	72.9	0.20	0.99	44.0	10.6	0.97
G7	Cd	28.0	0.16	0.99	43.0	10.0	0.83
G-Ca	Cr	71.0	0.18	0.98	46.2	9.8	0.95
G-Ca	Cd	28.0	0.14	0.98	44.5	9.2	0.85
G-Mn	Cr	76.0	0.22	0.99	48.8	10.5	0.96
G-Mn	Cd	32.0	0.18	0.99	46.1	10.1	0.88
G-Co	Cr	82.0	0.25	0.99	52.4	11.2	0.98
G-Co	Cd	36.0	0.21	0.99	49.3	10.8	0.92
G-Al	Cr	86.0	0.28	1.00	58.6	12.4	0.99
G-Al	Cd	38.0	0.24	1.00	54.2	11.9	0.94

3.4.2. Freundlich isotherm. The Freundlich model describes adsorption on heterogeneous surfaces with non-uniform energy distributions and allows for multilayer adsorption.[27] The model is expressed as:

$$q_e = k_F C_e^{1/n} \quad (8)$$

where K_F [(mg g^{-1})(L mg^{-1})$^{1/n}$] is the Freundlich adsorption capacity constant and $1/n$ is the adsorption intensity. A value of $n > 1$ indicates favourable adsorption. The linearized form, $\ln q_e = \ln K_F + (1/n) \ln C_e$, was used to extract K_F and n from the slope and intercept of the plot. Cr(VI) adsorption on G7 conformed well to the Freundlich model ($R^2 = 0.97$), suggesting heterogeneous surface adsorption consistent with multilayer formation. In contrast, Cd(II) adsorption on G7 showed a poor Freundlich fit ($R^2 = 0.83$), confirming that the Langmuir model provides a more accurate description for cadmium. The Freundlich constant n ranged from 9.2 to 12.4 across all samples, confirming highly favourable adsorption thermodynamics. The simultaneous applicability of both Langmuir and Freundlich models to Cr(VI) adsorption suggests that chromate ions interact with both homogeneous and heterogeneous surface sites, resulting in a combination of mono- and multilayer adsorption.

3.5. Treatment of produced water

Produced water co-generated with crude oil and natural gas constitutes the largest volume waste stream in petroleum exploration and production operations, often exceeding the volume of oil and gas produced by a factor of ten or more. Its composition comprising dissolved and dispersed hydrocarbons, suspended solids, heavy metals, and inorganic salts poses significant environmental and operational challenges, particularly in regions with escalating water scarcity such as Egypt. Two produced water samples from oil fields in the Gulf of Suez were treated under optimized batch adsorption conditions: adsorbent mass = 10 mg, temperature = 30 °C, pH = 6.0, solution volume = 25 mL, contact time = 60 min (Table 1). The results demonstrated removal to below FAAS detection limit of all detected heavy metals Cr, Mn, Cd, and Pb from both water samples using G7. The initial concentrations of Cr, Mn, Cd, and Pb in Produced Water 1 were 1.8, 1.17, 9.7, and 19.95 mg L^{-1}, respectively; in Produced Water 2, concentrations were below or at trace levels for most metals. The complete removal of heavy metals at the milligram-per-liter levels present in these samples, achieved under mild operating conditions and using a relatively small adsorbent mass, underscores the high specific adsorption capacity and selectivity of goethite nanomaterials for a broad spectrum of heavy metals. The performance of goethite in real matrix conditions where competing ions (Na^+, Ca^{2+}, Cl^-, SO_4^{2-}) are present is particularly noteworthy and suggests a strong inner-sphere complexation mechanism that is relatively insensitive to ionic competition. These results demonstrate that goethite nanomaterials represent a cost-effective and scalable alternative to expensive ion-exchange resins and semi-permeable membrane technologies for the treatment of heavy metal-contaminated industrial effluents.

3.6. Proposed adsorption mechanism

Based on the adsorption kinetics, isotherm analysis, pH dependence, and structural characterization data, the following surface complexation mechanisms are proposed for the adsorption of Cd^{2+} and Cr(VI) onto goethite-based adsorbents.

For divalent cadmium, adsorption proceeds *via* ligand exchange at the goethite surface, wherein Cd^{2+} displaces protons from reactive surface hydroxyl groups to form stable inner-sphere surface complexes.[28,29] At low to moderate pH, monodentate complexes are preferentially formed:

$$\equiv Fe\text{–}OH + Cd^{2+} \rightarrow \equiv Fe\text{–}O\text{–}Cd^{+} + H^{+} \text{ (Monodentate complex)}$$

At higher pH, the availability of adjacent surface sites promotes the formation of stronger bidentate surface complexes:

$$2\equiv Fe\text{–}OH + Cd^{2+} \rightarrow (\equiv Fe\text{–}O)_2Cd + 2H^{+} \text{ (Bidentate complex)}$$

The simultaneous presence of two types of terminal hydroxyl groups on the goethite surface hydroxo (–OH) and aqua (–OH_2)—provides further flexibility for both mono- and bidentate coordination modes.[30]

For hexavalent chromium, adsorption proceeds *via* anion exchange, in which chromate anions (CrO_4^{2-}) displace hydroxide groups from the goethite surface through an inner-sphere complexation mechanism, releasing OH^- into solution and increasing the solution pH:[31]

$$2\equiv Fe\text{–}OH + CrO_4^{2-} \rightarrow (\equiv Fe^{-})_2CrO_4 + 2OH^{-}$$

This inner-sphere exchange mechanism results in strong, selective binding of chromate to the goethite surface, explaining the high adsorption capacities and favorable isotherm parameters observed across all adsorbent samples. The enhanced performance of Al-goethite is attributable to the increased density of reactive surface hydroxyl sites generated by Al incorporation, as confirmed by FTIR analysis, which amplifies the capacity for both inner-sphere complexation (Cd^{2+}) and anion exchange (Cr(VI)).

It should be acknowledged that post-adsorption characterization of the spent adsorbents including zeta potential, DLS, and FTIR or XRD analysis was not performed in the present study, which represents a limitation. However, the adsorption mechanisms proposed herein are supported by, (i) the kinetic and isotherm modelling results confirming chemisorption and monolayer surface complexation; (ii) the static zeta potential and surface hydroxyl group data for the fresh adsorbents; (iii) the complete heavy metal removal achieved from complex produced water matrices containing competing ions; and (iv) extensive literature precedent for inner-sphere complexation of Cd^{2+} and Cr(VI) on goethite surfaces confirmed by direct spectroscopic techniques.[21,26] Future studies will incorporate post-adsorption FTIR, zeta potential, and DLS measurements to

provide direct experimental confirmation of the proposed surface interactions.

3.7. Adsorbent regeneration and green desorption strategies

While dilute mineral acids and alkalis represent the most widely reported eluents for regeneration of iron oxyhydroxide adsorbents, their use generates secondary waste streams that require neutralization and disposal, an acknowledged limitation from a green chemistry perspective. Several more sustainable regeneration strategies have been reported in the recent literature and are directly applicable to the FeO(OH)-based adsorbents developed in this study: electrochemical regeneration: the application of a mild anodic potential (0.5–1.5 V *vs.* Ag/AgCl) to the spent adsorbent has been demonstrated to desorb surface-bound metal ions through electrochemically induced pH shifts at the electrode–adsorbent interface, without the addition of chemical reagents.[32] This approach generates no secondary chemical waste and is compatible with renewable energy sources. Mild organic acid eluents: naturally derived organic acids such as citric acid and oxalic acid both biodegradable and environmentally benign have been shown to effectively desorb Cd^{2+} and Cr(VI) from iron oxyhydroxide surfaces through competitive complexation and ligand exchange, respectively, at concentrations as low as 0.05–0.1 M.[33] The resulting metal-loaded organic acid eluate can be further processed by electrodeposition or chemical precipitation to recover the heavy metals as reusable materials, closing the resource loop. Photocatalytic regeneration: For Cr(VI)-loaded adsorbents specifically, UV or solar irradiation in the presence of a sacrificial electron donor (*e.g.*, citric acid, formic acid) has been shown to reduce surface-bound Cr(VI) to Cr(III), which subsequently desorbs from the now-positively-charged goethite surface under mild acidic conditions enabling simultaneous Cr detoxification and adsorbent regeneration.[34] Supercritical CO_2 extraction: emerging supercritical fluid-based regeneration methods using CO_2, which is non-toxic, non-flammable, and recyclable, have demonstrated promising desorption efficiencies for heavy metal-loaded adsorbents without generating liquid waste streams.[35]

Among these alternatives, electrochemical regeneration and mild organic acid elution represent the most immediately implementable and scalable options for the FeO(OH)-based adsorbents developed in this study, and are recommended as priorities for investigation in future work aimed at developing a fully circular and sustainable heavy metal removal process for produced water treatment.

4. Conclusions

This study demonstrates the successful synthesis and application of pristine and metal-incorporated goethite (FeO(OH)) nanomaterials for the efficient removal of cadmium (Cd^{2+}) and hexavalent chromium (Cr(VI)) from aqueous solutions and real industrial produced water. The metal incorporation (Ca, Al, Co, Mn) into the goethite framework was confirmed by XRD, FTIR, HR-TEM, BET, and TGA/DTA analyses. Al incorporation produced the most pronounced structural effects, dispersing the goethite needle morphology, increasing specific surface area and zeta potential, and enriching the surface with reactive hydroxyl groups. Among all adsorbents tested, Al-goethite (G-Al) exhibited the highest adsorption capacities for both metals: q_m = 86 mg L^{-1} for Cr(VI) and 38 mg L^{-1} for Cd^{2+}, representing improvements of 18% and 36%, respectively, over pristine goethite (G7). The superior performance of G-Al is primarily attributed to its wider pore structure, higher surface area, and enhanced ionic potential of Al^{3+} at surface binding sites. Adsorption kinetics for both metals on all adsorbents conformed to the pseudo-second-order model ($R^2 \geq 0.98$), confirming a chemisorption mechanism involving electron exchange between metal ions and goethite surface hydroxyl groups. Equilibrium data were best described by the Langmuir isotherm for Cd^{2+} ($R^2 = 0.99$), indicating monolayer adsorption on the (001) and (010) goethite crystal faces. Cr(VI) adsorption conformed to both Langmuir and Freundlich models, consistent with mixed mono- and multilayer surface coverage on heterogeneous sites. The produced water treatment experiments were conducted as single measurements ($n = 1$), and results are reported conservatively as removal of Cr, Mn, Cd, and Pb to below the FAAS instrument detection limit. This is acknowledged as a limitation; future work will incorporate triplicate analyses with full statistical reporting to provide rigorous quantitative validation of the removal efficiencies demonstrated herein. These materials represent a promising alternative to conventional expensive treatment technologies such as ion-exchange resins and membrane separation processes, demonstrating their strong practical potential as cost-effective, scalable adsorbents for industrial wastewater remediation.

Author contributions

S. Said: conceptualization, methodology, investigation, formal analysis, data curation, writing – original draft, writing – review & editing, visualization, validation, supervision, resources, project administration, funding acquisition. H. H. El-Maghrabi: conceptualization, methodology, investigation, formal analysis, data curation, writing – original draft, writing – review & editing, visualization, validation, supervision, resources, project administration, funding acquisition. M. Riad: conceptualization, methodology, investigation, formal analysis, data curation, writing – original draft, writing – review & editing, visualization, validation, supervision, resources, project administration, funding acquisition. S. Mikhail: conceptualization, methodology, investigation, formal analysis, data curation, writing – original draft, writing – review & editing, visualization, validation, supervision, resources, project administration, funding acquisition.

Conflicts of interest

The authors declare that they have no known competing financial interests or personal relationships that could have influenced the work reported in this paper.

Data availability

The data supporting this article have been included as part of the Supplementary Information (SI). Supplementary information is available. See DOI: https://doi.org/10.1039/d6ra03786k.

Acknowledgements

The authors declare that this research received no specific grant from any funding agency in the public, commercial, or not-for-profit sectors.

References

1 N. P. Sibiya, T. P. Mahlangu, E. K. Tetteh and S. Rathilal, Review on advancing heavy metals removal: The use of iron oxide nanoparticles and microalgae-based adsorbents, *Cleaner Chem. Eng.*, 2025, **11**, 100137.
2 B. O. Yusuf, *et al.*, Comprehensive technologies for heavy metal remediation: Adsorption, membrane processes, photocatalysis, and AI-driven design, *Desalination*, 2025, 119261.
3 H. K. Herath, J. V Cizdziel, B. F. Platt and I. H. Widanagamage, Potential removal of heavy metal ions from polluted water using Bauxite, *Environ. Adv.*, 2023, **12**, 100362.
4 E. B. Hussein, F. A. Rasheed, A. S. Mohammed and K. F. Kayani, Emerging nanotechnology approaches for sustainable water treatment and heavy metals removal: a comprehensive review, *RSC Adv.*, 2025, **15**(48), 41061–41107.
5 A. M. Abdelaal, *12th International Conference on Mining, Petroleum and Metallurgical Engineering (MPM12)*, 2014, CODE MIN 07-2014.
6 L. K. Wang, D. A. Vaccari, Y. Li, and N. K. Shammas, Chemical precipitation, in *Physicochemical Treatment Processes*, Springer, 2005, pp. 141–197.
7 N. Karimian, M. I. Pownceby, E. D. Burton and A. J. Frierdich, Phosphorus–goethite interactions: A review of mechanisms, environmental implications, and industrial relevance, *Sci. Total Environ.*, 2026, **1012**, 181114.
8 Z. Wang, M. Mann, J. L. Hamilton, J. L. Wykes and A. J. Frierdich, Comparison between Co (II) and Ni (II) cycling at goethite-water interfaces: Interplay with Fe (II)-catalyzed recrystallization, *Geochim. Cosmochim. Acta*, 2024, **384**, 128–139.
9 R. Mohammed, H. H. El-Maghrabi, A. A. Younes, A. B. Farag, S. Mikhail and M. Riad, SDS-goethite adsorbent material preparation, structural characterization and the kinetics of the manganese adsorption, *J. Mol. Liq.*, 2017, **231**, 499–508.
10 R. Mohamed, H. H. El-Maghrabi, M. Riad and S. Mikhail, Environmental friendly FeOOH adsorbent materials preparation, characterization and mathematical kinetics adsorption data, *J. Water Process Eng.*, 2017, **16**, 212–222.
11 Z. Liu, J. Hao, X. Zhang and G. Wang, Enhanced chlorine activation on Cu-doped goethite via the synergistic effect of Cu+ and oxygen vacancy for efficient organic pollutant degradation, *Environ. Surf. Interfaces*, 2025, 18–27.
12 Y. Li and E. Bi, Mn-or Zn-substituted goethite enhancing tetracycline degradation by increasing oxygen vacancies and promoting electron transfer, *Colloids Surf., A*, 2024, **697**, 134374.
13 C. Tao, K. Wu, T. Liu, S. Yang and Z. Li, One-step removal of p-arsanilic acid via constructing bifunctional Zr-CuO/α-FeOOH catalyst: Efficient peroxymonosulfate activation, cooperative oxidation and adsorption, *Chem. Eng. J.*, 2025, **512**, 162285.
14 H. Qiu, L. Lv, B. Pan, Q. Zhang, W. Zhang and Q. Zhang, Critical review in adsorption kinetic models, *J. Zhejiang Univ. - Sci. A Appl. Phys. Eng.*, 2009, **10**(5), 716–724.
15 R. M. Cornell and U. Schwertmann, *The Iron Oxides: Structure, Properties, Reactions, Occurrences and Uses*, John Wiley & Sons, 2003.
16 Y. Zhao, J. Geng, X. Wang, X. Gu and S. Gao, Adsorption of tetracycline onto goethite in the presence of metal cations and humic substances, *J. Colloid Interface Sci.*, 2011, **361**(1), 247–251.
17 O. A. Oyewo, S. Makgato, H. Ferjani, C. Amairia, D. C. Onwudiwe and S. Abdalla, 1D α-FeO (OH) and its transformation to α-Fe2O3 nanorods: Synthesis and photocatalytic evaluation using bromocresol green, *Inorg. Chem. Commun.*, 2025, **175**, 114147.
18 F. A. Andersen, *et al.*, Infrared spectra of amorphous and crystalline calcium carbonate, *Acta Chem. Scand.*, 1991, **45**(10), 1018–1024.
19 J. Pedrosa, B. F. O. Costa, A. Portugal and L. Durães, Controlled phase formation of nanocrystalline iron oxides/hydroxides in solution–An insight on the phase transformation mechanisms, *Mater. Chem. Phys.*, 2015, **163**, 88–98.
20 V. V. Nenonen, *et al.*, Effects of organic ligands, phosphate and Ca on the structure and composition of Fe (III)-precipitates formed by Fe (II) oxidation at near-neutral pH, *Environ. Sci. Process. Impacts*, 2025, **27**(8), 2479–2506.
21 S. Fendorf, M. J. Eick, P. Grossl and D. L. Sparks, Arsenate and chromate retention mechanisms on goethite. 1. Surface structure, *Environ. Sci. Technol.*, 1997, **31**(2), 315–320.
22 M. Kosmulski, pH-dependent surface charging and points of zero charge. IV. Update and new approach, *J. Colloid Interface Sci.*, 2009, **337**(2), 439–448.
23 N. Galvez, V. Barron and J. Torrent, Preparation and properties of hematite with structural phosphorus, *Clays Clay Miner.*, 1999, **47**(3), 375–385.
24 R. E. Mesmer and C. F. Baes Jr, Review of hydrolysis behavior of ions in aqueous solutions, *MRS Online Proc. Libr.*, 1990, **180**(1), 85.
25 Y.-S. Ho and G. McKay, Pseudo-second order model for sorption processes, *Process Biochem.*, 1999, **34**(5), 451–465.
26 P. R. Grossl, M. Eick, D. L. Sparks, S. Goldberg and C. C. Ainsworth, Arsenate and chromate retention mechanisms on goethite. 2. Kinetic evaluation using

a pressure-jump relaxation technique, *Environ. Sci. Technol.*, 1997, **31**(2), 321–326.

27 K. Rout, A. Dash, M. Mohapatra and S. Anand, Manganese doped goethite: structural, optical and adsorption properties, *J. Environ. Chem. Eng.*, 2014, **2**(1), 434–443.

28 J. D. Ostergren, G. E. Brown Jr, G. A. Parks and P. Persson, Inorganic ligand effects on Pb (II) sorption to goethite (α-FeOOH): II. Sulfate, *J. Colloid Interface Sci.*, 2000, **225**(2), 483–493.

29 J. D. Filius, T. Hiemstra and W. H. Van Riemsdijk, Adsorption of small weak organic acids on goethite: Modeling of mechanisms, *J. Colloid Interface Sci.*, 1997, **195**(2), 368–380.

30 R. Strauss, G. W. Brümmer and N. J. Barrow, Effects of crystallinity of goethite: II. Rates of sorption and desorption of phosphate, *Eur. J. Soil Sci.*, 1997, **48**(1), 101–114.

31 A. Jaiswal, S. Banerjee, R. Mani and M. C. Chattopadhyaya, Synthesis, characterization and application of goethite mineral as an adsorbent, *J. Environ. Chem. Eng.*, 2013, **1**(3), 281–289.

32 M. El Gamal, H. A. Mousa, M. H. El-Naas, R. Zacharia and S. Judd, Bio-regeneration of activated carbon: A comprehensive review, *Sep. Purif. Technol.*, 2018, **197**, 345–359.

33 S. Babel and T. A. Kurniawan, Low-cost adsorbents for heavy metals uptake from contaminated water: a review, *J. Hazard. Mater.*, 2003, **97**(1–3), 219–243.

34 M. I. Litter, Last advances on TiO2-photocatalytic removal of chromium, uranium and arsenic, *Curr. Opin. Green Sustainable Chem.*, 2017, **6**, 150–158.

35 C.-H. Weng and M.-C. Hsu, Regeneration of granular activated carbon by an electrochemical process, *Sep. Purif. Technol.*, 2008, **64**(2), 227–236.